Check for updates

Highly active and stable surface structure for oxygen evolution reaction originating from balanced dissolution and strong connectivity in BaIrO₃ solid solutions†

Shigeto Hirai, [ID] *[a] Shunsuke Yagi, [ID] [b] He-Chan Oh,[a] Yoshiki Sato,[a] Wei Liu, [ID] [b] En-Pei Liu,[c] Wei-Tin Chen, [ID] [cd] Akira Miura, [ID] [e] Masanori Nagao, [ID] [f] Tomoya Ohno[a] and Takeshi Matsuda[a]

Catalysts for the oxygen evolution reaction (OER) are receiving great interest since OER remains the bottleneck of water electrolyzers for hydrogen production. Especially, OER in acidic solutions is crucial since it produces high current densities and avoids precipitation of carbonates. However, even the acid stable iridates undergo severe dissolution during the OER. BaIrO₃ has the strongest IrO₆ connectivity and stable surface structure, yet it suffers from lattice collapse after OER cycling, making it difficult to improve the OER durability. In the present study, we have successfully developed an OER catalyst with both high intrinsic activity and stability under acidic conditions by preventing the lattice collapse after repeated OER cycling. Specifically, we find that the substitution of Ir-site with Mn for BaIrO₃ in combination with OER cycling leads to a remarkable activity enhancement by a factor of 28 and an overall improvement in stability. This dual enhancement of OER performance was accomplished by the novel strategy of slightly increasing the Ir-dissolution and balancing the elemental dissolution in $BaIr_{1-x}Mn_xO_3$ to reconstruct a rigid surface with BaIrO₃-type structure. More importantly, the mass activity for $BaIr_{0.8}Mn_{0.2}O_3$ reached ~73 times of that for IrO₂, making it a sustainable and promising OER catalyst for energy conversion technologies.

1. Introduction

The oxygen evolution reaction (OER) is a crucial reaction for emerging energy conversion technologies such as electrochemical water splitting[1,2] and rechargeable metal–air batteries.[3,4] Since OER remains to be the bottleneck of water electrolyzers for hydrogen production that can be operated by renewable energy sources producing high current densities and avoiding precipitation of carbonates (CO_2 poisoning), OER catalysts in acidic solutions are receiving great interest.[5,6]

[a]School of Earth, Energy and Environmental Engineering, Kitami Institute of Technology, 165 Koen-cho, Kitami 090-8507, Japan. E-mail: hirai@mail.kitami-it.ac.jp

[b]Institute of Industrial Science, The University of Tokyo, 4-6-1 Komaba Meguro-ku, Tokyo 153-8505, Japan

[c]Center for Condensed Matter Sciences and Center of Atomic Initiative for New Materials, National Taiwan University, Taipei 10617, Taiwan

[d]Taiwan Consortium of Emergent Crystalline Materials, Ministry of Science and Technology, Taipei 10622, Taiwan

[e]Graduate School of Chemical Sciences and Engineering and Faculty of Engineering, Hokkaido University, Sapporo 060-8628, Japan

[f]University of Yamanashi, 7-32 Miyamae, Kofu, Yamanashi 400-0021, Japan

† Electronic supplementary information (ESI) available. See https://doi.org/10.1039/d2ra04624e

Recent discoveries of transition metal oxide-based catalysts[7–16] in both acidic and alkaline solutions have greatly advanced our understanding about the OER, revealing new OER mechanisms[17–19] and numerous OER descriptors.[20–22] However, particularly for catalysts in acidic solutions, it remains difficult to find the descriptors for OER and the underlying mechanism due to the dynamic nature of the oxide surface, which undergoes severe dissolution and amorphization during the OER. Such surface dissolution and amorphization of OER catalysts usually leads to the decrease of intrinsic OER activity or low stability, even for acid stable iridium and ruthenium metal oxide-based catalysts.[23–27] In addition, the kinetics of the OER becomes even more sluggish because of the multistep electron transfer process,[4] and the possible OER mechanisms are still under discussion. Thus, finding OER catalysts with both high activity and stability in acidic solutions is a crucial and challenging task. Accordingly, catalyst discovery in acidic solutions must begin with the most stable iridium-based oxide (iridate) catalysts before moving on to the generally less stable 3d transition metal oxide catalysts.

Recently, Song *et al.*[27] systematically studied the OER performance of three groups of iridates in 0.5 M H_2SO_4 aqueous solution, revealing the relationship between IrO₆ octahedral

connectivity and OER stability. Among the three groups of iridates, BaIrO$_3$ with strong IrO$_6$ connectivity (dominated by the face-sharing octahedra) exhibited the highest OER stability, while SrIrO$_3$ with intermediate IrO$_6$ connectivity (a mixture of face-sharing and corner-sharing octahedra) exhibited moderate OER stability and Ba$_4$Ir$_3$O$_{10}$ with weak IrO$_6$ connectivity (dominated by the corner-sharing clusters) exhibited the lowest OER stability. Furthermore, the recent OER study about BaIrO$_3$ synthesized by solution calcination has demonstrated its excellent OER performance due to the high valence of Ir (Ir^{5+}) in the IrO$_x$ surface layer.[28] However, despite being one of the most stable OER catalysts, BaIrO$_3$ (with strong IrO$_6$ connectivity) experiences a decrease in intrinsic OER activity (OER current density normalized to the electrochemically active surface area) with cycling,[27,28] and the OER activity per oxide begins to decrease after repeated cycling due to the substantial dissolution of IrO$_6$ units. This dissolution of IrO$_6$ units originates from the lattice collapse (specifically at the surface amorphous layer) of BaIrO$_3$ particles and leads to the loss of intrinsic OER activity (such lattice collapse takes place at a much earlier stage of OER for SrIrO$_3$ due to its weaker IrO$_6$ connectivity). In other words, the lattice collapse of the surface amorphous layer occurs sooner or later because its chemical bonding (of the IrO$_6$ units) is weaker than that of the crystalline layer. Therefore, the lattice collapse of iridate particles[27] after repeated OER cycling is a challenging issue to overcome, and further reduction of Ir-dissolution may not be a viable option since BaIrO$_3$ has the strongest IrO$_6$ octahedral connectivity (dominated by the face-sharing octahedra) among iridates.

In the present study, we have prevented the lattice collapse of BaIrO$_3$ catalyst by substituting the Ir-site with Mn and succeeded in developing an OER catalyst with both high intrinsic activity and stability. This was achieved by the novel strategy of slightly increasing the Ir-dissolution and balancing the elemental dissolution in BaIr$_{1-x}$Mn$_x$O$_3$ to reconstruct a rigid BaIrO$_3$-type structure at the surface amorphous layer (Mn is at the same crystallographic site as Ir, and it will induce the Ir-dissolution since Mn is easier to dissolve during the OER under acidic conditions). Specifically, the OER activities of the isostructural BaIr$_{1-x}$Mn$_x$O$_3$ ($0 \leq x \leq 0.3$) solid solutions were systematically studied, and a remarkable activity enhancement by a factor of 28 and an overall improvement in stability was achieved by the balanced elemental dissolution and strong IrO$_6$ octahedral connectivity in BaIr$_{1-x}$Mn$_x$O$_3$. In concrete, both high intrinsic OER activity and high OER stability in acidic solutions was enabled by the robust and thin surface layer of BaIr$_{1-x}$Mn$_x$O$_3$, which was formed by the good balance between Ba- and Ir-dissolution, and the strong IrO$_6$ connectivity of BaIrO$_3$-type structure. Thus, our study suggests that BaIr$_{1-x}$M$_x$O$_3$ solid solutions (M: 3d transition metal) provide a promising venue for the development of highly active and durable OER catalysts in acidic environment.

2. Experimental

2.1 Sample synthesis and characterization

Polycrystalline samples of BaIr$_{1-x}$Mn$_x$O$_3$ ($x = 0$, 0.1, 0.2, and 0.3) were synthesized by solid state reaction from BaCO$_3$ (Wako

Pure Chemical Industries Ltd.), IrO$_2$ (Wako Pure Chemical Industries Ltd.) and Mn$_3$O$_4$. The purpose of this study is to compare the OER activity of BaIr$_{1-x}$Mn$_x$O$_3$ with that of BaIrO$_3$ within the robust structural regime of BaIrO$_3$. Therefore, we focused on the composition ($x = 0$, 0.1, 0.2, and 0.3) that BaIr$_{1-x}$Mn$_x$O$_3$ adopts the crystal structure isostructural with BaIrO$_3$ (in the space group of $C12/m1$). Mn$_3$O$_4$ powder was prepared from MnCO$_3$ (Kojundo Chemical Laboratory) by heating in air at 1000 °C for 18 h. Well-ground mixtures of the starting materials in the stoichiometric ratio were heated in air at 900 °C for 12 h, followed by regrinding and heating at 1000 °C for a total of 73 h as in Zhao *et al.*[29]

The phase purity and lattice constants of the BaIr$_{1-x}$Mn$_x$O$_3$ ($x = 0$, 0.1, 0.2, and 0.3) powders were examined by powder X-ray diffraction (XRD) (Rigaku; RINT2500Ultra18) using Cu Kα radiation ($\lambda = 1.540598$ Å) at RT, and the structures were refined *via* the Rietveld method starting from the crystal structure of BaIrO$_3$ in JCPDS #01-080-1880 using the GSAS Rietveld refinement software.[30] Also, the synchrotron X-ray powder diffraction profile of BaIrO$_3$ was obtained at the TPS19A beamline, National Synchrotron Radiation Research Center (NSRRC) with 15 keV beam and the MYTHEN detector in order to check the validity of the zero position and the lattice constants obtained by powder X-ray diffraction. Scanning electron microscopy with energy-dispersive X-ray analysis (SEM/EDX) was conducted using a JEOL JSM-6701F at an acceleration voltage of 20 kV. High-resolution transmission electron microscopy (HRTEM) measurements were conducted using a JEOL JEM-2100. The valence state and the chemical bonding of BaIr$_{1-x}$Mn$_x$O$_3$ ($x = 0$, 0.1, 0.2, and 0.3) samples were examined by X-ray absorption near-edge structure (XANES) and extended X-ray absorption fine structure (EXAFS) spectra collected in transmission mode at Aichi synchrotron BL5S1. After the data collection, XANES and EXAFS spectra were analyzed with the software of Ifeffit Athena and Artemis.[31]

2.2 Electrochemical measurements

The catalyst inks for the electrochemical measurements were prepared referring to methods reported by Suntivich *et al.*[12] and Grimaud *et al.*[13] K$^+$ ion-exchanged Nafion® was used as an immobilizing binder, enabling smooth transport of dissolved O$_2$ to the surface of the catalysts. A 3.33 wt% K$^+$ ion-exchanged Nafion® suspension was first obtained from a mixture of 5 wt% proton-type Nafion® suspension (Sigma-Aldrich) and a 0.1 M KOH aqueous solution in a 2 : 1 (v/v) ratio. This process increased the pH of the initial 5 wt% proton-type Nafion® suspension from 1–2 to 11. The catalyst inks were prepared from a mixture of the as-prepared samples (25 mg), acetylene black (AB, Strem Chemicals Inc., 5 mg) and 3.33 wt% K$^+$ ion-exchanged Nafion® suspension (1.5 mL). The total ink volumes were adjusted to 5 mL by the addition of tetrahydro-furan (Sigma-Aldrich), to give final concentrations of 5 mg sample per mL, 1 mg AB per mL, and 1 mg Nafion per mL in the ink. A sample of the ink (6.4 μL) was then drop-casted on a rotating-ring disk electrode composed of a glassy carbon (GC) disk ($0.2 \times 0.2 \times \pi$ cm^2) and a Pt ring (BAS Inc., Japan), which

Paper

was used as the working electrode after mirror polishing with 0.05 μM alumina slurry (BAS Inc., Japan). The catalyst layer on the GC disk was dried overnight in vacuum at room temperature, and was composed of 0.25 mg sample per cm_{disk}^2, 0.05 mg AB per cm_{disk}^2 and ~0.05 mg Nafion per cm_{disk}^2.

Electrochemical measurements were conducted using a rotating ring disk electrode rotator (RRDE-3A, BAS Inc., Japan) at 1600 rpm, in combination with a bipotentiostat (BAS Inc., Japan). In addition, a Pt wire counter electrode, and an Hg/Hg_2SO_4 reference electrode (BAS Inc., Japan) filled with 0.5 M H_2SO_4 aqueous solution (Wako, Ltd., Japan) were used. Electrochemical measurements were conducted with O_2 saturation (30 min bubbling O_2 gas through the solution). During OER current measurements for each sample, the potential of the sample-modified GC was controlled from 0.53 to 0.95 V vs. Hg/Hg_2SO_4 with an internal solution of 0.5 M H_2SO_4 (1.228–1.648 V vs. RHE) at 10 mV s^{-1}. For all measurements, the OER current density was iR-corrected ($R = \sim 8$ Ω) using the measured solution resistance, and capacitance-corrected by averaging the anodic and cathodic scans[12] to remove the non-faradaic current contribution. The current densities (mA cm_{oxide}^{-2} and mA cm_{disk}^{-2}) were obtained by dividing the OER current with the oxide BET surface area and the glassy carbon disk electrode area. The electrochemical impedance spectra (EIS) were measured in the frequency range between 200 kHz and 100 mHz at the amplitude of 10 mV.

3. Results and discussion

3.1 OER activity of $BaIr_{1-x}Mn_xO_3$

The OER activity of $BaIr_{1-x}Mn_xO_3$ ($x = 0$, 0.1, 0.2, and 0.3) was studied in 0.5 M H_2SO_4 aqueous solutions. We selected this range of Mn content to exclude any structural effect on OER performance and to preserve the strong IrO_6 octahedral connectivity of the OER stable $BaIrO_3$ (ref. 27 and 32) denoted as '9M'[29] (that is a monoclinically distorted version of $BaRuO_3$ (ref. 33)). We confirmed by X-ray diffraction that $BaIr_{1-x}Mn_xO_3$ adopts a monoclinic structure with the space group of $C12/m1$ (Fig. 1a and b), which is isostructural with $BaIrO_3$ (also see the XRD profiles in Fig. S1† and crystallographic information in Table S1 and Fig. S2†). $BaIr_{1-x}Mn_xO_3$ particles are in the size of 1–3 μm (see the SEM images in Fig. S3 and S4†). Mn content x was determined by EDX (Fig. S3†) and the relationship between Mn content and lattice volume (Fig. S2b†), and its validity was tested with the Ir and Mn valence confirmed by the X-ray absorption near-edge structure (XANES) spectra (Fig. S5a and S7a†).

Capacitance-corrected voltammograms (0.53 to 0.95 V vs. Hg/Hg_2SO_4 filled with 0.5 M H_2SO_4) for $BaIr_{1-x}Mn_xO_3$ ($x = 0$, 0.1, 0.2, and 0.3) are shown in Fig. 2a, while the corresponding cyclic voltammograms are depicted in Fig. S9a.† For the majority of catalysts, including $SrIrO_3$,[27] the lattice collapse and the elemental dissolution is severe during the OER, and OER current density begins to decrease after repeated cycling due to the loss of intrinsic OER activity (current density normalized to the electrochemically active surface area) even when the electrochemically active surface area (ECSA) increases
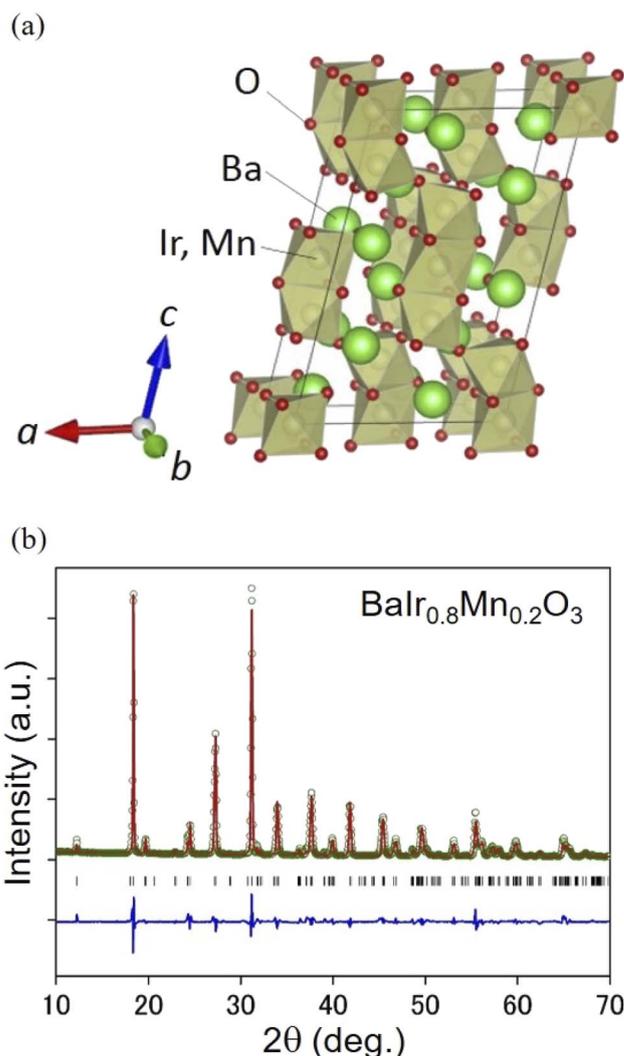

Fig. 1 (a) Schematic representation of the crystal structure of $BaIr_{1-x}Mn_xO_3$. This image was drawn using the VESTA software.[38] $BaIr_{1-x}Mn_xO_3$ ($x = 0$, 0.1, 0.2, and 0.3) adopts a monoclinic structure with the space group of $C12/m1$, which is characterized by the ionic coordination denoted as '9M'[29] (monoclinically distorted version of $BaRuO_3$ with the ionic coordination of 9R[33]) with a zigzag network of three face-sharing IrO_6 (MnO_6) octahedra forming columns. (b) The representative XRD profile and Rietveld refinement result of $BaIr_{1-x}Mn_xO_3$ ($x = 0.2$). The green circles and the red line indicate the observed and calculated profile, respectively. The blue line displays the difference between the observed and calculated profile. The black tick marks indicate the Bragg reflection positions of $BaIr_{0.8}Mn_{0.2}O_3$. Wavelength $\lambda = 1.540598$ Å.

due to surface amorphization. In contrast, the OER current density of $BaIrO_3$ continues to increase over a long cycle (200 to 1000 OER cycles depending on the potential range) as a result of the intense chemical bonding (enabled by the strong IrO_6 connectivity) that minimizes the loss of intrinsic OER activity and the sharp increase of ECSA that originates from the thick IrO_x amorphous layer.[27] Thus, in this paper, we will evaluate the $BaIr_{1-x}Mn_xO_3$ catalyst that has experienced 1000 OER cycles as a separate OER catalyst (from pristine catalyst) because the final surface structure after OER is more crucial than the initial
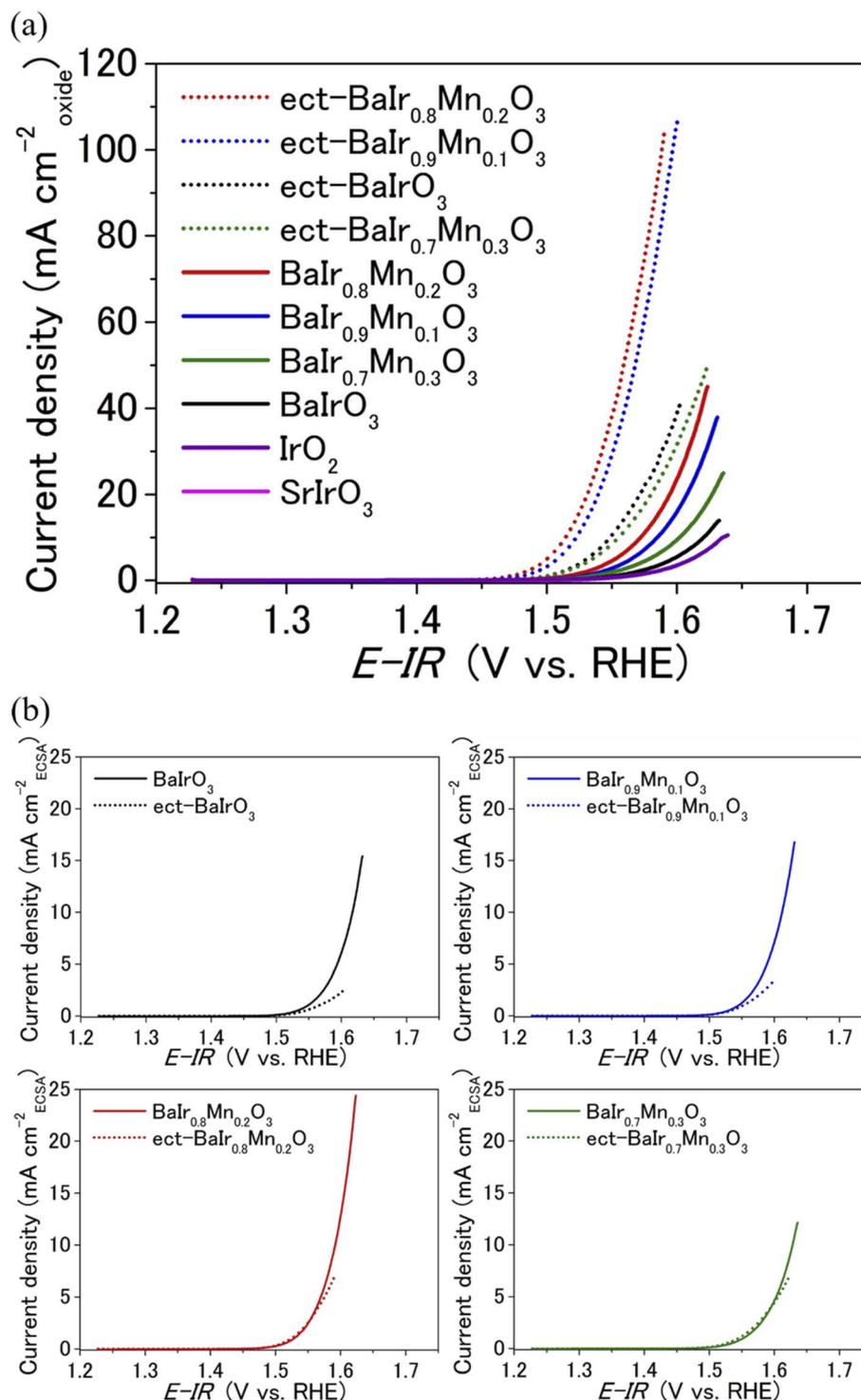
Fig. 2 (a) Linear sweep voltammograms (LSV) for pristine and electrochemically treated (ect-) $BaIr_{1-x}Mn_xO_3$ ($x = 0$, 0.1, 0.2, and 0.3) in 0.5 M H_2SO_4 aqueous solution normalized to the oxide surface area in Table S2.† LSV of $SrIrO_3$ is overlapping with that of IrO_2. (b) LSV for pristine and electrochemically treated (ect-) $BaIr_{1-x}Mn_xO_3$ ($x = 0$, 0.1, 0.2, and 0.3) normalized to the relative ECSA determined from the slope of Fig. S10c.†

surface structure for $BaIr_{1-x}Mn_xO_3$. For simplicity, each $BaIr_{1-x}Mn_xO_3$ catalyst after 1000 OER cycles will be referred to as ect-$BaIr_{1-x}Mn_xO_3$ (abbreviation for electrochemically treated $BaIr_{1-x}Mn_xO_3$). It is clear from Fig. 2a and S11† that neither the OER activity per oxide surface area (see the details of BET surface area in Table S2†) nor the OER activity per geometrical electrode area (see also Fig. S9b†) for $BaIr_{1-x}Mn_xO_3$ varies monotonically with the Mn content. Instead, the OER activities of the $BaIr_{1-x}Mn_xO_3$ solid solution ($0.1 \leq x \leq 0.2$) are significantly higher than those of $BaIrO_3$ for both pristine and

electrochemically treated samples. This is also the case for other parameters describing the OER performance of $BaIr_{1-x}Mn_xO_3$ (see the relationship between Mn content and OER descriptors in Fig. S16†). As evident from the cyclic voltammograms in Fig. S9a,† the double-layer capacitance of $BaIrO_3$ shows a sharp increase after 1000 OER cycles, while that of $BaIr_{1-x}Mn_xO_3$ does not show a rapid increase after 1000 OER cycles. Therefore, it is important to calculate the OER activity normalized to the ECSA for the comparison of intrinsic OER activity and the evaluation of OER cyclic stability over the long term. Since the chemical composition is similar in pristine and electrochemically treated samples, ECSA is proportional to the double-layer capacitance within each chemical composition of $BaIr_{1-x}Mn_xO_3$ ($x = 0, 0.1, 0.2,$ and 0.3). For this reason, we evaluate the intrinsic OER activity of $BaIr_{1-x}Mn_xO_3$ in Fig. 2b by normalizing to the relative ECSA (that is proportional to the double-layer capacitance in Fig. S10c†), which is defined by the following ratio: ECSA of electrochemically treated $BaIr_{1-x}Mn_xO_3$/ECSA of pristine $BaIr_{1-x}Mn_xO_3$. Furthermore, we should limit the comparison of intrinsic OER activity in Fig. 2b to potentials below 1.57 V *vs.* RHE since the coverage of the catalytic surface by O_2 bubbles cannot be ignored above 1.57 V *vs.* RHE (the electrode potential with 20 mA cm_{geo}^{-2} for electrochemically treated $BaIrO_3$) for the electrochemically treated samples, and dividing the current density above 1.57 V *vs.* RHE with the ECSA calculated from the potential range below 1.57 V *vs.* RHE will underestimate the intrinsic OER activity. In particular, when the current density is normalized to the relative ECSA, the intrinsic OER activity of electrochemically treated samples for $BaIr_{0.8}Mn_{0.2}O_3$ and $BaIr_{0.7}Mn_{0.3}O_3$ below 1.57 V *vs.* RHE is comparable to that of pristine samples (Fig. 2b). On the other hand, electrochemically treated $BaIrO_3$ shows a 50% decrease in intrinsic OER activity relative to pristine sample at 1.57 V *vs.* RHE due to the lattice collapse of the surface structure.[27] Similarly, electrochemically treated $BaIr_{0.9}Mn_{0.1}O_3$ shows a 30% decrease in intrinsic OER activity relative to pristine sample at the same potential (Fig. 2b). Therefore, the remarkably high OER activity of electrochemically treated $BaIr_{0.8}Mn_{0.2}O_3$ originates from the well maintained intrinsic OER activity during 1000 OER cycles. At an applied potential of 1.58 V *vs.* RHE, a current density of 85 mA cm^{-2} (Fig. 3a) was recorded for electrochemically treated $BaIr_{0.8}Mn_{0.2}O_3$ with a small charge transfer resistance of ~16 Ω in Table S3d† (this value is obtained by fitting the electrochemical impedance spectra of Fig. S13a,† and it is smaller than the value of $BaIrO_3$ in Tables S3a and S3c†). This indicates that the observed high current density comes from the OER. The observed current density for electrochemically treated $BaIr_{0.8}Mn_{0.2}O_3$ is ~28 times higher than that for pristine $BaIrO_3$, ~3.5 times higher than that for electrochemically treated $BaIrO_3$, ~46 times higher than that for $SrIrO_3$, and ~45 times higher than that for IrO_2 (we note that $BaIrO_3$ is one of the most stable OER catalysts with high current density, and the initial OER activity of $SrIrO_3$ is comparable with that of pristine $BaIrO_3$ (ref. 27)). As shown in Fig. 2b, this trend is maintained even when the current density is normalized to the relative ECSA. In other words, the comparison of OER activity for $BaIr_{1-x}Mn_xO_3$ (Fig. 2a and 3a) is not biased by the surface area or by the number of

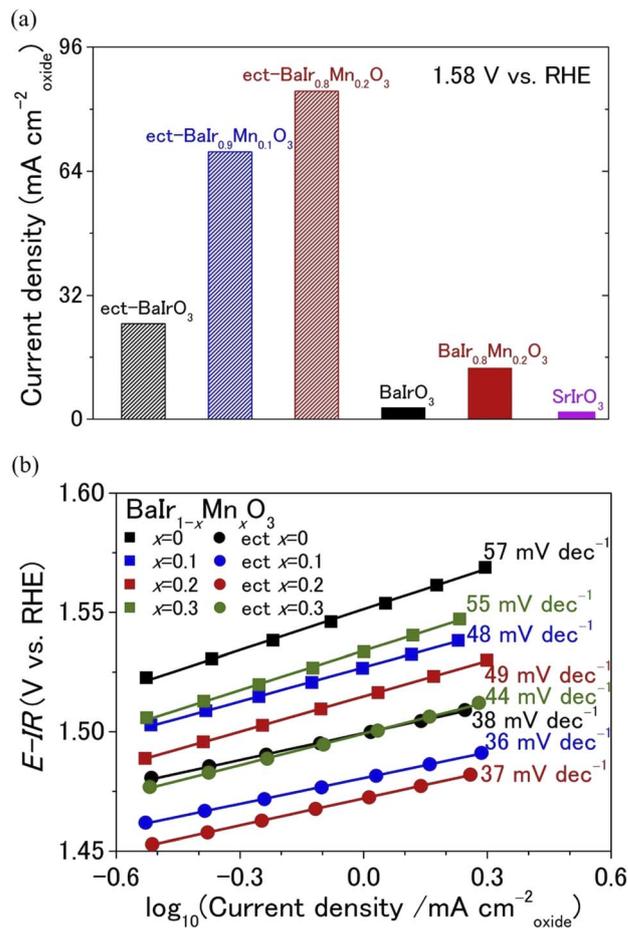**Fig. 3** (a) The representative OER current density at 1.58 V *vs.* RHE for pristine and electrochemically treated (ect-) $BaIr_{1-x}Mn_xO_3$ in 0.5 M H_2SO_4 aqueous solution. The current density of $SrIrO_3$ is shown for comparison. By the way, the current density of IrO_2 is ~1.9 mA cm_{oxide}^{-2} at 1.58 V *vs.* RHE, which is obtained from Fig. 2a. (b) Tafel plots for pristine and electrochemically treated (ect-) $BaIr_{1-x}Mn_xO_3$ ($x = 0, 0.1, 0.2,$ and 0.3) collected under steady-state conditions.

accessible active sites. Furthermore, Table S4† demonstrates that the electrochemically treated $BaIr_{0.8}Mn_{0.2}O_3$ and $BaIr_{0.9}Mn_{0.1}O_3$ show 60–100 times higher turnover frequency (TOF) than that of IrO_2, and 10–20 times higher TOF than that of $SrIrO_3$ (here, TOF was calculated by TOF = $J/4Fn$, where J is the OER current at 1.58 V *vs.* RHE, F is the Faraday constant, and n is the number of moles of the Ir atom on the working electrode). Fig. 3b shows the *iR*-corrected Tafel plots obtained under steady-state conditions for pristine and electrochemically treated $BaIr_{1-x}Mn_xO_3$. $BaIr_{1-x}Mn_xO_3$ ($x = 0, 0.1, 0.2,$ and 0.3) exhibited Tafel slopes of 36–44 mV dec^{-1} for electrochemically treated samples, and 48–57 mV dec^{-1} for pristine samples. The smaller Tafel slope in Fig. 3b and the lower onset potential in Fig. 2a and S11† demonstrate that both pristine and electrochemically treated $BaIr_{0.8}Mn_{0.2}O_3$ and $BaIr_{0.9}Mn_{0.1}O_3$ exhibit higher OER activity than $BaIrO_3$ and other iridates, such as IrO_2 and $SrIrO_3$. Consequently, we have demonstrated that electrochemically treated $BaIr_{0.8}Mn_{0.2}O_3$ and $BaIr_{0.9}Mn_{0.1}O_3$ show excellent overall OER performance. Next, we will investigate the

reason for the extremely high OER activity of $BaIr_{0.8}Mn_{0.2}O_3$ and the high cyclic stability of $BaIr_{1-x}Mn_xO_3$ ($0.1 \leq x \leq 0.3$). We note that the trend of OER activity in $BaIr_{1-x}Mn_xO_3$ (depicted in Fig. 2a, b, and S16†) cannot be explained by the difference of Ir–O bond distance (see the Ir–O bond distance of Table S1† obtained by the EXAFS fitting in Fig. S6,† and the successful Mn K-edge EXAFS fitting). Instead, the relatively longer Ir–O bond distance of electrochemically treated $BaIrO_3$ suggests the existence of a weaker Ir–O bonding at the $BaIrO_3$ surface after repeated OER cycling, which is consistent with the thick amorphous layer observed in the transmission electron microscopy image of Fig. 4b (that will be explained in detail in the next paragraph). Therefore, the highest OER activity at $x \sim 0.2$ and the high overall OER activity of $BaIr_{1-x}Mn_xO_3$ ($0.1 \leq x \leq 0.3$) must be explained by a descriptor other than Ir–O covalency or orbital hybridization (Table S1†).

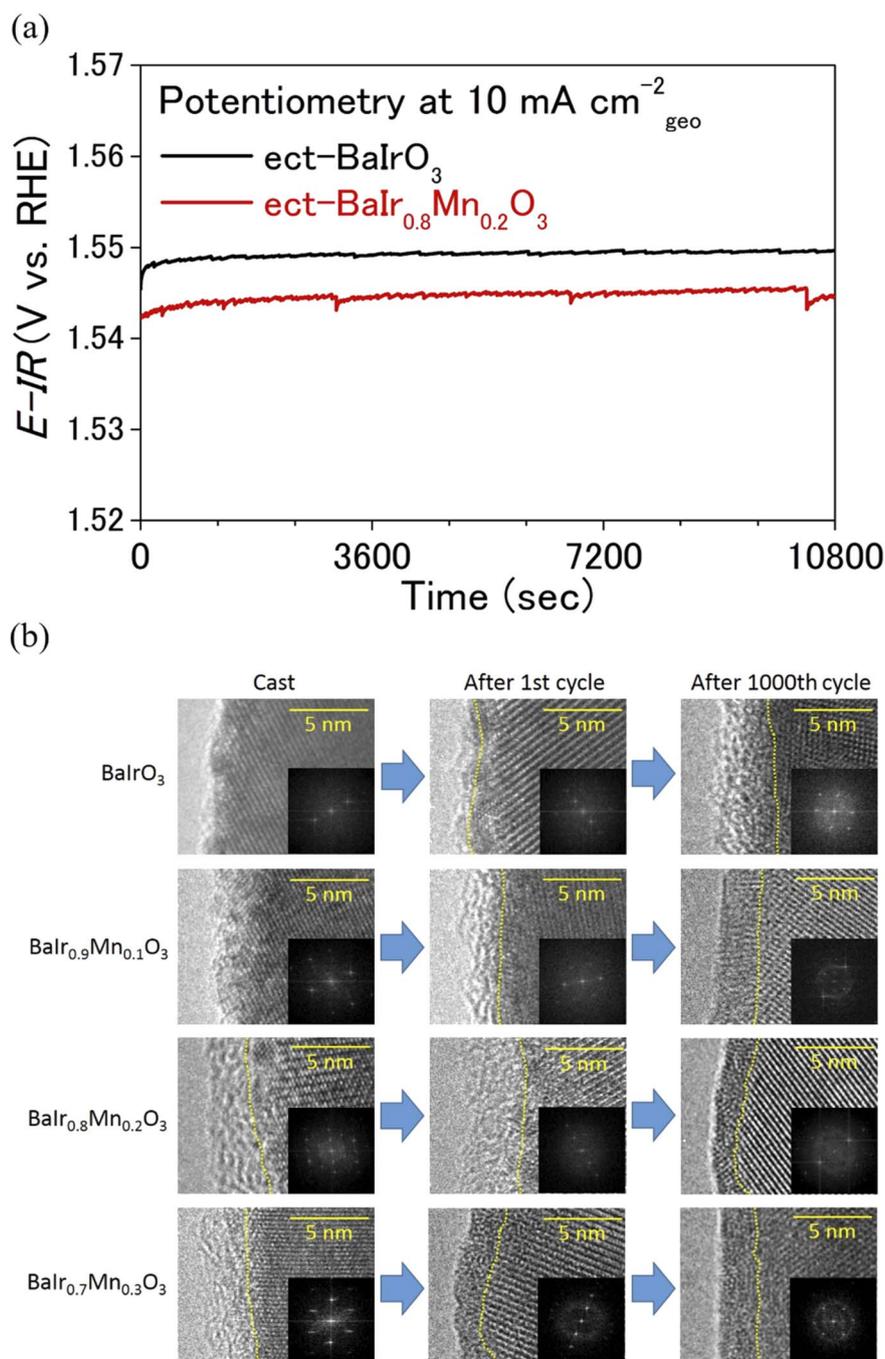**Fig. 4** (a) Chronopotentiometric curves at 10 mA cm$_{geo}^{-2}$ (current density normalized to the geometrical electrode area) for electrochemically treated (ect-) $BaIr_{0.8}Mn_{0.2}O_3$ and $BaIrO_3$. (b) The OER catalytic surface of $BaIr_{1-x}Mn_xO_3$. HRTEM and fast Fourier transform (FFT) images of as-cast, after 1st and 1000 OER cycles for $BaIr_{1-x}Mn_xO_3$ ($x = 0$, 0.1, 0.2, and 0.3) are shown. The boundaries between the crystalline layer and the amorphous layer are divided by yellow dotted lines.

3.2 OER stability of $BaIr_{1-x}Mn_xO_3$

Extended electrochemical studies were conducted to investigate the catalytic stability of $BaIr_{1-x}Mn_xO_3$ ($x = 0$, 0.1, 0.2, and 0.3). The chronopotentiometric curve depicted in Fig. 4a demonstrates that the OER activity of $BaIr_{0.8}Mn_{0.2}O_3$ is stable in 0.5 M H_2SO_4 with the polarization potential being nearly constant (at a geometrical current density of 10 mA cm^{-2}) for 3 h, while remaining lower than that of $BaIrO_3$. Moreover, it is evident from the inductively coupled plasma optical emission spectroscopy (ICP-OES) result (see the elemental concentration in Table S5†) after 1000 OER cycles that the bulk dissolution during the OER is negligible and $BaIr_{1-x}Mn_xO_3$ ($x = 0.1$, 0.2, and 0.3) is an exceptionally stable OER catalyst. This high OER stability of $BaIr_{1-x}Mn_xO_3$ ($x = 0$, 0.1, 0.2, and 0.3) was further probed using high-resolution transmission electron microscopy (HRTEM) for both pristine and electrochemically treated samples (including the samples after the first OER cycle). Fig. 4b shows the HRTEM and fast Fourier transform (FFT) images of $BaIr_{1-x}Mn_xO_3$ before and after OER measurements (also see the expansion of FFT images in Fig. S14†). Before discussing the catalytic stability in detail, we note that, as reported by Yagi et al.[14] and May et al.,[34] the catalytic activity of an OER catalyst is determined by the ~10 nm layer of the catalytic surface. For the as-cast sample, $BaIrO_3$ possesses a highly-crystalline surface structure. However, after the first OER cycle, a 1–2 nm amorphous layer is observed at the catalytic surface, and after 1000 OER cycles, the amorphous layer finally develops to ~5 nm thickness (Fig. 4b), which eventually leads to the lattice collapse of the surface structure.[27] In contrast, $BaIr_{1-x}Mn_xO_3$ solid solutions ($x = 0.1$, 0.2, and 0.3) show 2–3 nm amorphous layer already after the first OER cycle, but the thickness of the amorphous layer decreases (in the case of $BaIr_{0.8}Mn_{0.2}O_3$) or remains nearly constant even after 1000 OER cycles. Furthermore, the amorphous layer of the $BaIr_{1-x}Mn_xO_3$ solid solution ($x = 0.1$, 0.2, and 0.3) in Fig. 4b shows somewhat crystalline stripes after 1000 OER cycles (which is not observed after the first OER cycle for $BaIr_{0.8}Mn_{0.2}O_3$ and $BaIr_{0.9}Mn_{0.1}O_3$), indicating the existence of a short-range atomic order at the outermost surface and the reconstruction of the catalytic surface (that is likely to be $Ba_{1-z}Ir_{1-y}Mn_yO_x$ units originating from the highly crystalline $BaIr_{1-x}Mn_xO_3$ layer beneath the amorphous layer). This observation of short-range atomic order (or the existence of long-range atomic order to some extent) suggests that the lattice collapse and subsequent loss of OER activity are prevented in the $BaIr_{1-x}Mn_xO_3$ solid solution ($x = 0.1$, 0.2, and 0.3) unlike the case for $BaIrO_3$ ($BaIrO_3$ suffers from lattice collapse after repeated OER cycling as reported by Song et al.[27]). We noted that these observations are in good agreement with the change of ECSA, which originates primarily from the ECSA of the amorphous layer at the catalytic surface. Based on Fig. S10c,† the relative ECSA after 1000 OER cycles is ~19 for $BaIrO_3$, while it is ~14 for $BaIr_{0.9}Mn_{0.1}O_3$, ~8.1 for $BaIr_{0.8}Mn_{0.2}O_3$, and ~3.5 for $BaIr_{0.7}Mn_{0.3}O_3$. With increasing Mn content, the relative ECSA continues to decrease, indicating that not only does the thickness of the amorphous layer decrease, but also the atomic order within the amorphous layer improves

(since the more crystalline surface has less ECSA). This change of ECSA is well reflected in the somewhat crystalline stripes of the thinner (relative to $BaIrO_3$) amorphous layers in $BaIr_{1-x}Mn_xO_3$ ($x = 0.1$, 0.2, and 0.3) (the feature of crystalline stripes is particularly evident for $x = 0.2$ and 0.3). We note that the amorphization mechanism of the Sr_yIrO_x surface layer demonstrated for the $SrIrO_3$ thin film grown on a $DyScO_3$ (110) orthorhombic substrate along the (001) pseudo-cubic orientation is another example of a non IrO_x unit at the catalytic surface,[35] while all of the $BaIr_{1-x}Mn_xO_3$ samples in this study were obtained by solid state synthesis. We also note that Mn and Ir occupy the same crystallographic site, and Mn-dissolution will induce Ir-dissolution because Mn is easier to dissolve under acidic conditions during the OER (yet Mn is among the OER stable elements under acidic conditions when it forms an oxide, and manganese oxides show higher stability than any other 3d transition metal oxides).[36] For this reason, the crystalline stripes after 1000 OER cycles (Fig. 4b) and the high OER stability for the $BaIr_{1-x}Mn_xO_3$ solid solution ($x = 0.1$, 0.2, and 0.3) in Fig. 5b and 4a may well be the result of a balanced surface dissolution of Ba- and Ir-site (Mn-site) that enables the formation of $Ba_{1-z}Ir_{1-y}Mn_yO_x$ units (instead of the Ir-rich IrO_x units) in combination with the strong IrO_6 connectivity of $BaIr_{1-x}Mn_xO_3$ (that protects the catalytic surface from suffering excessive Ir-site dissolution and therefore minimizes the particle size reduction during the OER). The well sustained intrinsic OER activity observed for electrochemically treated $BaIr_{0.8}Mn_{0.2}O_3$ and $BaIr_{0.7}Mn_{0.3}O_3$ in Fig. 2b below 1.57 V vs. RHE is in good agreement with this surface reconstruction (observed as crystalline stripes), while the 30% decrease of intrinsic OER activity observed for electrochemically treated $BaIr_{0.9}Mn_{0.1}O_3$ may suggest that the surface reconstruction only proceeds partially when the surface dissolution of Ir is insufficient (due to the lack of Mn) and does not balance with the surface dissolution of Ba. Here, we demonstrate the scenario of the surface structure of $BaIr_{1-x}Mn_xO_3$ after repeated OER cycling in Fig. 5a, which is consistent with the high intrinsic OER activity and high stability of the $BaIr_{1-x}Mn_xO_3$ solid solution ($x = 0.1$, 0.2, and 0.3) after 1000 OER cycles shown in Fig. 2b and 5b. We stress that the fresh (meaning that the chemical composition is similar to the initial $BaIr_{1-x}Mn_xO_3$) and robust amorphous layer that is formed at the catalytic surface is the key for the high intrinsic OER activity and high stability of $BaIr_{1-x}Mn_xO_3$ ($x = 0.1$, 0.2, and 0.3). This is in contrast to $SrIrO_3$, in which the peeling off of the surface structure (just like the skin of an onion) leads to the loss of intrinsic OER activity due to the particle size reduction caused by the weaker IrO_6 connectivity (that is a mixture of face-sharing and corner-sharing octahedra) at amorphous layer. In concrete, $BaIrO_3$ and $BaIr_{1-x}Mn_xO_3$ ($x = 0.1$, 0.2, and 0.3) possesses a zigzag network of three face-sharing IrO_6 octahedra forming columns that is characteristic for the 9M ionic coordination, while $SrIrO_3$ possesses two face-sharing IrO_6 octahedra separated by single IrO_6 octahedra characteristic for the 6M ionic coordination (Fig. 5a), and thereby the IrO_6 connectivity is weaker for $SrIrO_3$. After repeated OER cycling, the surface structure of IrO_2 resembles that of $SrIrO_3$, and it is reported that the surface
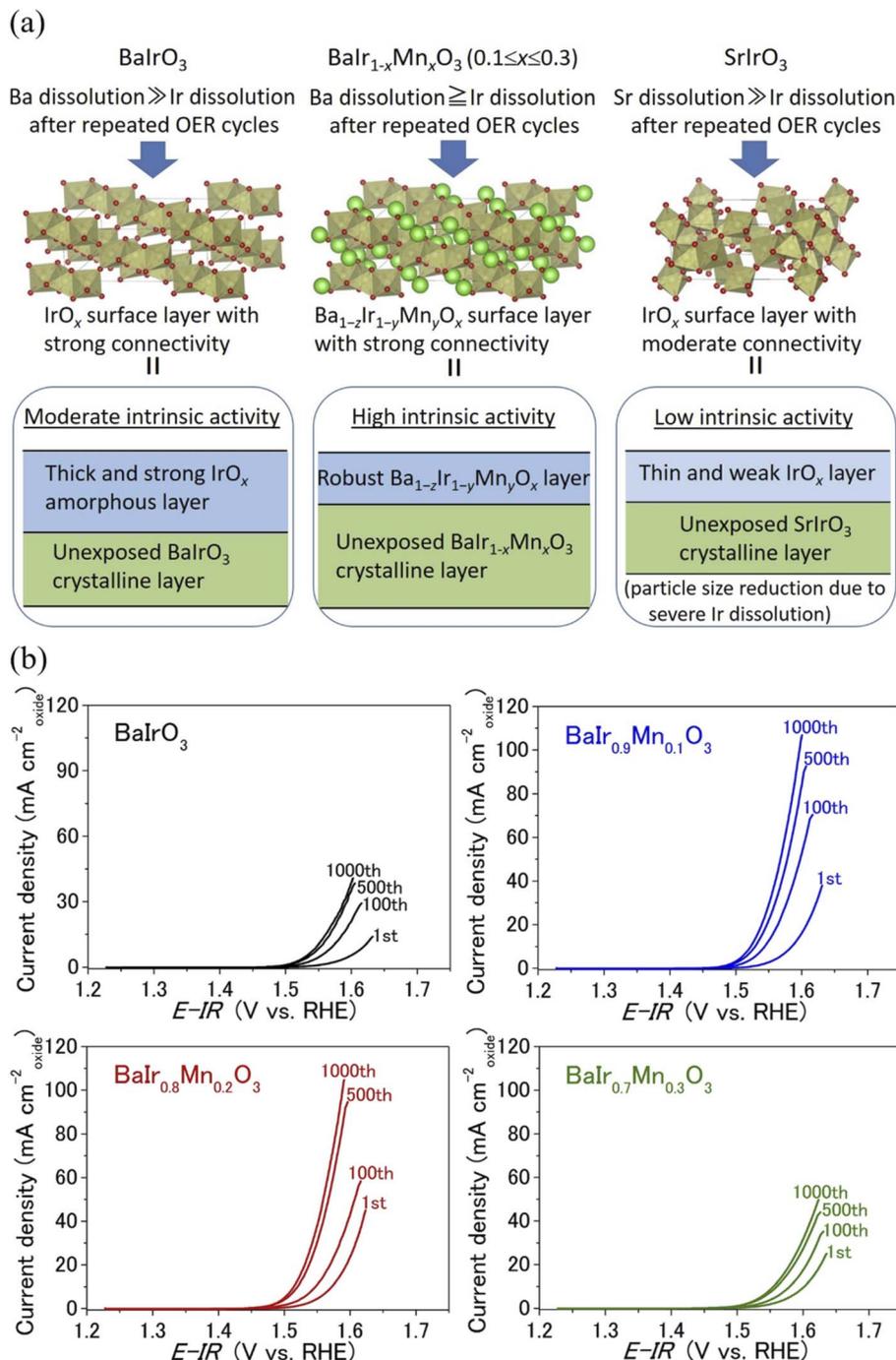
Fig. 5 (a) Schematic representation of the surface structure in $BaIr_{1-x}Mn_xO_3$ after repeated OER cycling. The surface structure image was drawn using the VESTA software.[38] The surface structure of $SrIrO_3$ is shown for comparison. (b) The cycle dependence of the linear sweep voltammograms for $BaIr_{1-x}Mn_xO_3$ (x = 0, 0.1, 0.2, and 0.3).

structure of IrO_2 belongs to the same group as that of $SrIrO_3$.[27] Moreover, the increase of Ir-dissolution in $BaIr_{1-x}Mn_xO_3$ compared to $BaIrO_3$ may appear to have a negative effect at first glance, but the peeling off of the surface structure by the balanced dissolution of Ba and Ir is easily relaxed after repeated OER cycling due to the strong IrO_6 connectivity, and the surface structure will be reconstructed in contrast to the case of $BaIrO_3$ (in which an Ir-rich amorphous layer keeps on growing at the

catalytic surface due to the unbalanced dissolution of Ba and Ir) and $SrIrO_3$ (in which the peeling off of the surface structure simply leads to the particle size reduction due to the weaker IrO_6 connectivity). Therefore, our new strategy of slightly increasing the Ir-dissolution and balancing the elemental dissolution in $BaIr_{1-x}Mn_xO_3$ for reconstructing a rigid $BaIrO_3$-type structure at the amorphous layer seems to be successful. The importance of the robust $BaIrO_3$-type structure for the

reconstruction of the surface layer is strongly supported by the low cyclic stability of $x = 0.4$ (see the severe decrease of current density after 1000 OER cycles in Fig. S12b†). As shown in the crystal structure of Fig. S12a,† as soon as the monoclinic distortion in $BaIr_{1−x}Mn_xO_3$ ($x = 0.1, 0.2,$ and 0.3) is lost and the structure transforms into the $BaRuO_3$-type structure for $BaIr_{0.6}Mn_{0.4}O_3$ (i.e., the chemical pressure decreases with the decrease of average ionic radius at the octahedral site and the crystal structure becomes less rigid), the intrinsic OER activity of $BaIr_{0.6}Mn_{0.4}O_3$ in Fig. S12c† shows a sharp decrease (at a much lower potential than $x = 0.1, 0.2,$ and 0.3) after 1000 OER cycles. In other words, not only the balanced elemental dissolution but also the rigid $BaIrO_3$-type structure of $BaIr_{1−x}Mn_xO_3$ is essential for the reconstruction of the robust amorphous layer at the catalytic surface.

3.3 Chemical state and further OER cycling of $BaIr_{1−x}Mn_xO_3$

Next, we will examine the surface structure scenario depicted in Fig. 5a from the standpoint of the chemical state of $BaIr_{1−x}Mn_xO_3$. The chemical state of $BaIr_{1−x}Mn_xO_3$ ($x = 0, 0.1, 0.2,$ and 0.3) was probed using X-ray absorption near-edge structure (XANES) and extended X-ray absorption fine structure (EXAFS) spectra for pristine and electrochemically treated samples (by 1000 OER cycles). As shown in the XANES spectra of Fig. 6a, for pristine samples, the valence of Ir remains 4+ throughout the system, while the valence of Mn is 4+ for $x = 0.1$ and a mixture of 3+ and 4+ for $x = 0.2$ and 0.3 (that is supported by the visible energy shift of the Mn absorption edge with respect to $BaMnO_3$ in Fig. S7a†). The presence of Mn^{3+} for $x = 0.2$ and 0.3 implies that Mn^{3+}-induced Ir dissolution (Mn–O bonding becomes weaker with the presence of Mn^{3+}) enables a good balance with the Ba-site dissolution of $BaIr_{1−x}Mn_xO_3$ ($0.1 \leq x \leq 0.3$) and leads to the emergence of $Ba_{1−z}Ir_{1−y}Mn_yO_x$ units at the surface layer, which possesses higher OER activity and stability than the Ir-rich IrO_x units formed at the $BaIrO_3$ surface (that experiences lattice collapse during the OER). This is consistent with the scenario depicted in Fig. 5a and suggests that Mn^{3+} drives the balanced dissolution of Ba and Ir in $BaIr_{1−x}Mn_xO_3$ ($0.1 \leq x \leq 0.3$). Simultaneously, too high concentrations of oxygen vacancies for $BaIr_{1−x}Mn_xO_3$ at high Mn content (caused by the high concentration of Mn^{3+}) may slightly increase the number of
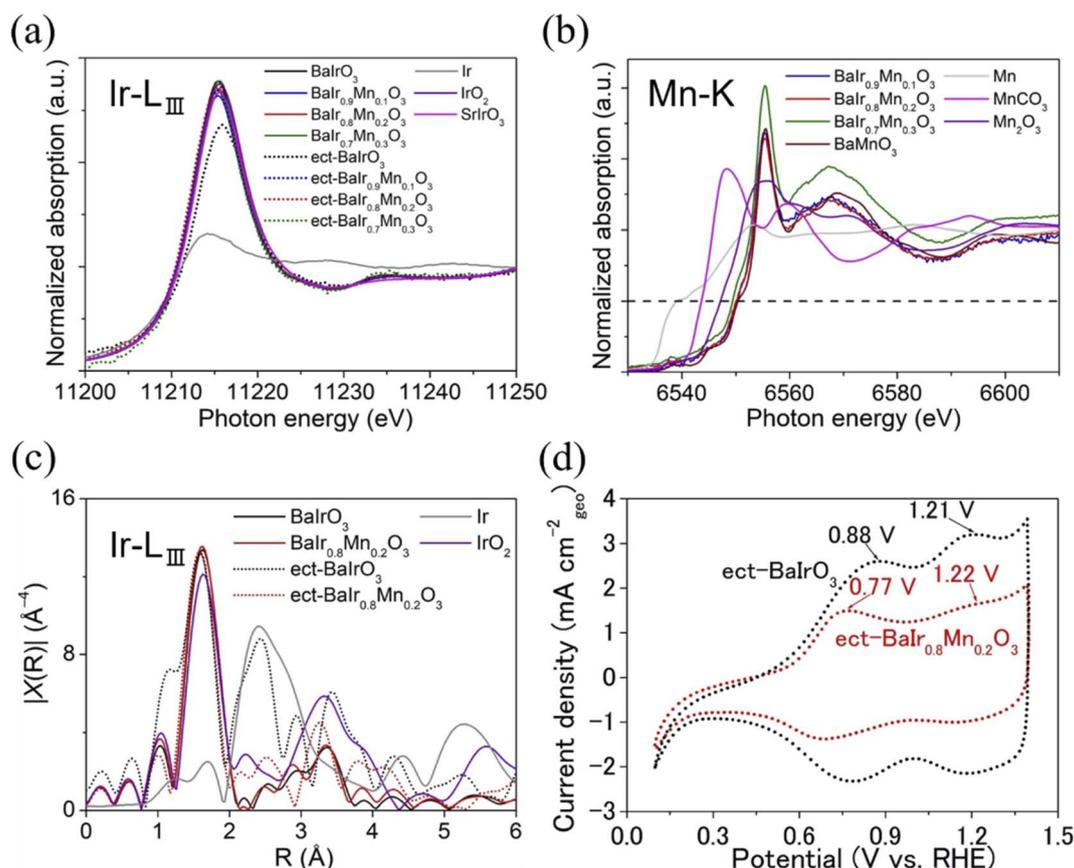

Fig. 6 (a) Normalized Ir L_{III}-edge X-ray absorption near-edge structure (XANES) spectra for pristine and electrochemically treated (ect-) $BaIr_{1−x}Mn_xO_3$ ($x = 0, 0.1, 0.2,$ and 0.3). Ir L_{III}-edge XANES spectra of Ir, IrO_2 and $SrIrO_3$ were collected for comparison. (b) Normalized Mn K-edge XANES spectra for pristine and electrochemically treated (ect-) $BaIr_{1−x}Mn_xO_3$ ($x = 0, 0.1, 0.2,$ and 0.3). Mn K-edge XANES spectra of Mn, $MnCO_3$, Mn_2O_3, and $BaMnO_3$ were collected as standard materials. For Mn K-edge XANES spectra, the dashed line is a guide for the energy position with the half height of the normalized edge height. (c) The representative Fourier transformed k^3-weighted Ir L_{III}-edge EXAFS for pristine and electrochemically treated (ect-) $BaIr_{1−x}MnxO_3$ in the representation form of $|X(R)|$. (d) The representative cyclic voltammograms for electrochemically treated (ect-) $BaIr_{1−x}Mn_xO_3$ measured from −0.6–0.7 V vs. Hg/Hg_2SO_4 at the scan rate of 100 mV $s^{−1}$.

active sites for OER, but it will also induce increased Ir-dissolution and result in the loss of initial OER activity. This is likely to be the reason for the lower initial activity of $x = 0.3$ compared with $x = 0.1$ and $x = 0.2$ in Fig. 2a. In contrast, $x = 0.2$ demonstrates the highest OER activity and stability owing to the combination of a good balance of elemental dissolution of Ba and Ir from the surface $Ba_{1-z}Ir_{1-y}Mn_yO_x$ units and the strong IrO_6 connectivity originating from the $BaIrO_3$-type structure. In other words, $BaIr_{0.8}Mn_{0.2}O_3$ realizes the ideal case for the surface structure of $BaIr_{1-x}Mn_xO_3$ (Fig. 5a). Next, we will examine the chemical state of Ir. The Ir L_{III}-edge white line of electrochemically treated $BaIr_{1-x}Mn_xO_3$ (Fig. 6b) shows either a stronger peak intensity or a slight energy shift with respect to pristine $BaIr_{1-x}Mn_xO_3$ (Fig. S5a†). Therefore, Ir^{4+} is partially oxidized to Ir^{5+} during the 1000 OER cycles. This is also consistent with the previously reported enhancement of OER activity by the high-valence Ir^{5+} of IrO_x formed as a $BaIrO_3$ surface layer.[28] As shown in the EXAFS spectra of Fig. 6c (also see the detailed version in Fig. S5b†), the pronounced peak between 2–3 Å ascribed to the Ir–Ir metal–metal bonding for Ir metal is present for $BaIrO_3$, while it is not present for $BaIr_{1-x}Mn_xO_3$ ($x = 0.1, 0.2,$ and 0.3). This suggests that the Ir-rich IrO_x units (in good consistency with the previous EXAFS study about iridium oxide OER catalysts[37]) are formed at the surface amorphous layer of electrochemically treated $BaIrO_3$, while the robust $Ba_{1-z}Ir_{1-y}Mn_yO_x$ framework is formed at the surface amorphous layer of electrochemically treated $BaIr_{1-x}Mn_xO_3$ ($x = 0.1, 0.2,$ and 0.3). This is also in good agreement with the scenario presented in Fig. 5a and suggests that the Ir-rich IrO_x unit is not formed at the surface layer of $BaIr_{1-x}Mn_xO_3$ ($x = 0.1, 0.2,$ and 0.3). We have also looked into the redox behavior of the $BaIr_{1-x}Mn_xO_3$ solid solution ($x = 0.1, 0.2,$ and 0.3). Fig. 6d and (the more detailed) Fig. S15† show cyclic voltammograms for detecting the redox behavior of the Ir-site in both pristine and electrochemically treated $BaIr_{1-x}Mn_xO_3$. The Ir oxidation peak of $BaIr_{1-x}Mn_xO_3$ appears at a lower or nearly identical potential to that of $BaIrO_3$ (the first oxidation peak corresponds to the oxidation from Ir^{3+} to Ir^{4+}, and the second oxidation peak corresponds to the oxidation from Ir^{4+} to Ir^{5+}), indicating that Mn is a redox-inactive element during the OER for the $BaIr_{1-x}Mn_xO_3$ solid solution as in the case of Zr for $SrIr_{2/3}Zn_{1/3}O_3$.[10] In other words, Ir^{4+} is partially oxidized to Ir^{5+} during the OER mainly due to the Ir-site dissolution in $BaIr_{1-x}Mn_xO_3$ (and not because of the valence change of Mn). The excellent OER performance of electrochemically treated (ect-) $BaIr_{0.8}Mn_{0.2}O_3$ was further examined by the extended OER stability test over 1000 cycles. As shown in Fig. 7a, the current density of electrochemically treated $BaIr_{0.8}Mn_{0.2}O_3$ does not decrease even after additional 1000 OER cycles, instead it shows slight increase due to an increase in electrochemical surface area (Fig. S17a and b†) caused by the slight progression of amorphization. Furthermore, the intrinsic OER activity of electrochemically treated $BaIr_{0.8}Mn_{0.2}O_3$ in Fig. S17c† (the current density normalized to the relative ECSA with respect to pristine $BaIr_{0.8}Mn_{0.2}O_3$, which is determined from Fig. S17b†) remains high after additional 1000 OER cycles and it is comparable with the initial activity below 1.57 V *vs.* RHE.
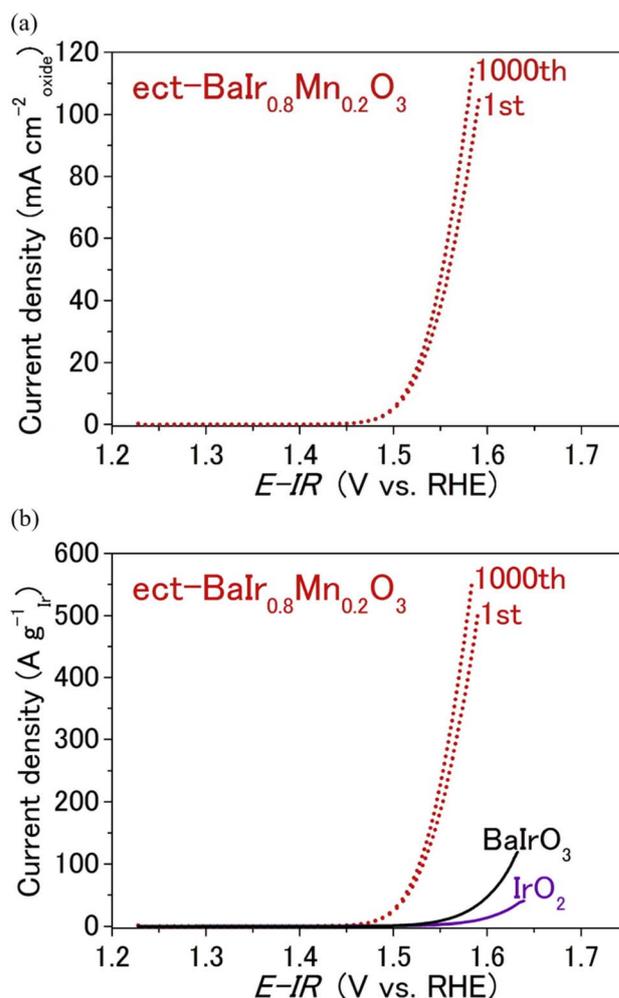

Fig. 7 (a) The cycle dependence of the linear sweep voltammograms for electrochemically treated (ect-) $BaIr_{0.8}Mn_{0.2}O_3$ in 0.5 M H_2SO_4 aqueous solution normalized to the oxide surface area. (b) The cycle dependence of the linear sweep voltammograms for electrochemically treated (ect-) $BaIr_{0.8}Mn_{0.2}O_3$ normalized to the mass of Ir. The mass activity of $BaIrO_3$ and IrO_2 are shown for comparison.

Therefore, electrochemically treated $BaIr_{0.8}Mn_{0.2}O_3$ demonstrates not only high OER stability during the potentiometric measurement, but also high cyclic stability owing to the high intrinsic OER activity even after 1000 OER cycles. More importantly, Fig. 7b shows that the OER activity per Ir mass at 1.58 V *vs.* RHE for electrochemically treated $BaIr_{0.8}Mn_{0.2}O_3$ eventually becomes ~25 times higher than that for pristine $BaIrO_3$, and ~73 times higher than that for IrO_2. This excellent mass activity of electrochemically treated $BaIr_{0.8}Mn_{0.2}O_3$ has important implications, as the Ir content of commercial IrO_2 can be drastically reduced without compromising OER performance. In conclusion, electrochemically treated $BaIr_{0.8}Mn_{0.2}O_3$ is not only a sustainable but also a highly active and an extremely stable OER catalyst benefitting from the reconstruction of the robust amorphous layer at the catalytic surface, which originates from the good balance between Ba- and Ir-dissolution, and the strong IrO_6 connectivity of the $BaIrO_3$-type structure.

4. Conclusion

In conclusion, we have prevented the lattice collapse after repeated OER cycling, which is an issue even for the acid stable iridates, by substituting the Ir-site of $BaIrO_3$ with Mn and successfully enhanced both the intrinsic OER activity and catalytic stability. Specifically, we find that $BaIr_{0.8}Mn_{0.2}O_3$ in combination with OER cycling shows remarkable activity enhancement by a factor of 28 and an overall improvement in stability. The trade-off relationship of activity and stability in OER catalysts is solved by the novel strategy of slightly increasing the Ir-dissolution and balancing the elemental dissolution in $BaIr_{1-x}Mn_xO_3$ for reconstructing a rigid $BaIrO_3$-type structure at the surface amorphous layer. Our finding suggests that both high intrinsic OER activity and high OER stability originate from the robust and thin surface layer of $BaIr_{1-x}Mn_xO_3$ that is constructed by the good balance between Ba- and Ir-dissolution, and the strong IrO_6 connectivity of the $BaIrO_3$-type structure. Moreover, the mass activity of $BaIr_{0.8}Mn_{0.2}O_3$ reached $\sim$73 times of that for IrO_2, making it a sustainable and promising OER catalyst for energy conversion technologies. The electrochemically treated $BaIr_{0.8}Mn_{0.2}O_3$ has not only broken the trade-off relationship of activity and stability in OER catalysts but also drastically reduced the Ir content of commercial IrO_2 without compromising the OER performance.

Author contributions

S. H. mainly conceived, designed and wrote this paper. S. Y. partially designed, co-wrote and contributed to this paper. O. H. and Y. S. synthesized the catalysts. S. H., O. H. and Y. S. conducted the electrochemical measurements. S. Y. and W. L. conducted the BET surface area measurements. E.-P. L. and W.-T. C. collected the synchrotron XRD profiles. A. M. conducted the ICP-OES measurements. M. N. and A. M. collected the XAS measurements. All authors discussed the results and commented on the manuscript.

Conflicts of interest

The authors declare no conflict of interest.

Acknowledgements

References

1 T. E. Mallouk, *Nat. Chem.*, 2013, **5**, 362–363.

2 F. M. Sapountzi, J. M. Gracia, C. J. Weststrate, H. O. A. Fredriksson and J. W. Niemantsverdriet, *Prog. Energy Combust. Sci.*, 2017, **58**, 1–35.

3 M. Armand and J. M. Tarascon, *Nature*, 2008, **451**, 652–657.

4 Y. C. Lu, Z. Xu, H. A. Gasteiger, S. Chen, K. Hamad-Schifferli and Y. Shao-Horn, *J. Am. Chem. Soc.*, 2010, **132**, 12170–12171.

5 M. Carmo, D. L. Fritz, J. Mergel and D. Stolten, *Int. J. Hydrogen Energy*, 2013, **38**, 4901–4934.

6 S. S. Kumar and V. Himabindu, *Mater. Sci. Energy Technol.*, 2019, **2**, 442–454.

7 O. Diaz-Morales, S. Raaijman, R. Kortlever, P. J. Kooyman, T. Wezendonk, J. Gascon, W. T. Fu and M. T. M. Koper, *Nat. Commun.*, 2016, 7, 12363.

8 L. Yang, G. Yu, X. Ai, W. Yan, H. Duan, W. Chen, X. Li, T. Wang, C. Zhang, X. Huang, J.-S. Chen and X. Zou, *Nat. Commun.*, 2018, **9**, 5236.

9 J. Chen, P. Cui, G. Zhao, K. Rui, M. Lao, Y. Chen, X. Zheng, Y. Jiang, H. Pan, S. X. Dou and W. Sun, *Angew. Chem., Int. Ed.*, 2019, **58**, 12540–12544.

10 X. Liang, L. Shi, R. Cao, G. Wan, W. Yan, H. Chen, Y. Liu and X. Zou, *Adv. Mater.*, 2020, **32**, 2001430.

11 Y. Lin, Z. Tian, L. Zhang, J. Ma, Z. Jiang, B. J. Deibert, R. Ge and L. Chen, *Nat. Commun.*, 2019, **10**, 162.

12 J. Suntivich, K. J. May, H. A. Gasteiger, J. B. Goodenough and Y. Shao-Horn, *Science*, 2011, **334**, 1383–1385.

13 A. Grimaud, K. J. May, C. E. Carlton, Y. L. Lee, M. Risch, W. T. Hong, J. Zhou and Y. Shao-Horn, *Nat. Commun.*, 2013, **4**, 2439.

14 S. Yagi, I. Yamada, H. Tsukasaki, A. Seno, M. Murakami, H. Fujii, H. Chen, N. Umezawa, H. Abe, N. Nishiyama and S. Mori, *Nat. Commun.*, 2015, **6**, 8249.

15 S. Hirai, S. Yagi, W.-T. Chen, F.-C. Chou, N. Okazaki, T. Ohno, H. Suzuki and T. Matsuda, *Adv. Sci.*, 2017, **4**, 1700176.

16 J. G. Lee, J. Hwang, H. J. Hwang, O. S. Jeon, J. Jang, O. Kwon, Y. Lee, B. Han and Y. G. Shul, *J. Am. Chem. Soc.*, 2016, **138**, 3541–3547.

17 A. Grimaud, O. Diaz-Morales, B. Han, W. T. Hong, Y.-L. Lee, L. Giordano, K. A. Stoerzinger, M. T. M. Koper and Y. Shao-Horn, *Nat. Chem.*, 2017, **9**, 457–465.

18 E. Fabbri, M. Nachtegaal, T. Binninger, X. Cheng, B.-J. Kim, J. Durst, F. Bozza, T. Graule, R. Schäublin, L. Wiles, M. Pertoso, N. Danilovic, K. E. Ayers and T. J. Schmidt, *Nat. Mater.*, 2017, **16**, 925–931.

19 Y. Y. Tian, S. Wang, E. Velasco, Y. P. Yang, L. J. Cao, L. J. Zhang, X. Li, Y. C. Lin, Q. J. Zhang and L. Chen, *iScience*, 2020, **23**, 100756.

20 W. T. Hong, R. E. Welsch and Y. Shao-Horn, *J. Phys. Chem. C*, 2016, **120**, 78–86.

21 S. Hirai, S. Yagi, A. Seno, M. Fujioka, T. Ohno and T. Matsuda, *RSC Adv.*, 2016, **6**, 2019–2023.

22 H. B. Tao, L. Fang, J. Chen, H. B. Yang, J. Gao, J. Miao, S. Chen and B. Liu, *J. Am. Chem. Soc.*, 2016, **138**, 9978–9985.

23 Y. Lin, Z. Tian, L. Zhang, J. Ma, Z. Jiang, B. J. Deibert, R. Ge and L. Chen, *Nat. Commun.*, 2019, **10**, 162.

24 M. Retuerto, L. Pascual, O. Piqué, P. Kayser, M. A. Salam, M. Mokhtar, J. A. Alonso, M. Peña, F. Calle-Vallejo and S. Rojas, *J. Mater. Chem. A*, 2021, **9**, 2980–2990.

25 J. Edgington, N. Schweitzer, S. Alayoglu and L. C. Seitz, *J. Am. Chem. Soc.*, 2021, **143**, 9961–9971.

26 Y. Chen, H. Li, J. Wang, Y. Du, S. Xi, Y. Sun, M. Sherburne, J. W. Ager III, A. C. Fisher and Z. J. Xu, *Nat. Commun.*, 2019, **10**, 572.

27 C. W. Song, J. Lim, H. B. Bae and S.-Y. Chung, *Energy Environ. Sci.*, 2020, **13**, 4178–4188.

28 N. Li, L. Cai, C. Wang, Y. Lin, J. Huang, H. Sheng, H. Pan, W. Zhang, Q. Ji, H. Duan, W. Hu, W. Zhang, F. Hu, H. Tan, Z. Sun, B. Song, S. Jin and W. Yan, *J. Am. Chem. Soc.*, 2021, **143**, 18001–18009.

29 J. G. Zhao, L. X. Yang, Y. Yua, F. Y. Li, R. C. Yu and C. Q. Jin, *J. Solid State Chem.*, 2010, **183**, 720–726.

30 A. C. Larson and R. B. von Dreele, *Los Alamos National Laboratory Report*, LAUR, 2000, pp. 86–748.

31 B. Ravel and M. Newville, *J. Synchrotron Radiat.*, 2005, **12**, 537–541.

32 T. Siegrist and B. L. Chamberland, *J. Less-Common Met.*, 1991, **170**, 93–99.

33 P. C. Donohue, L. Katz and R. Ward, *Inorg. Chem.*, 1965, **4**, 306–310.

34 K. J. May, C. E. Carlton, K. A. Stoerzinger, M. Risch, J. Suntivich, Y. L. Lee, A. Grimaud and Y. Shao-Horn, *J. Phys. Chem. Lett.*, 2012, **3**, 3264–3270.

35 G. Wan, J. W. Freeland, J. Kloppenburg, G. Petretto, J. N. Nelson, D.-Y. Kuo, C.-J. Sun, J. Wen, J. T. Diulus, G. S. Herman, Y. Dong, R. Kou, J. Sun, S. Chen, K. M. Shen, D. G. Schlom, G.-M. Rignanese, G. Hautier, D. D. Fong, Z. Feng, H. Zhou and J. Suntivich, *Sci. Adv.*, 2021, **7**, eabc7323.

36 M. Huynh, C. Shi, S. J. L. Billinge and D. G. Nocera, *J. Am. Chem. Soc.*, 2015, **137**, 14887–14904.

37 G. Kwon, S. H. Chang, J. E. Heo, K. J. Lee, J.-K. Kim, B.-G. Cho, T. Y. Koo, B. J. Kim, C. Kim, J. H. Lee, S.-M. Bak, K. A. Beyer, H. Zhong, R. J. Koch, S. Hwang, L. M. Utschig, X. Huang, G. Hu, G. W. Brudvig, D. M. Tiede and J. Kim, *ACS Catal.*, 2021, **11**, 10084–10094.

38 K. Momma and F. Izumi, *J. Appl. Crystallogr.*, 2011, **44**, 1272–1276.